metals

Article

Microstructural Evolution and Protection Behavior of CoCrNiTiAl Nanocrystalline–Amorphous Composite Structure Films

Lei Huang [1,2], Zonglin Li [3], Xin Shen [3], Wei Jiang [3,*], Lingjie Chen [1,2,*] and Longbo Li [1,2]

[1] State Key laboratory of Marine Corrosion and Protection, Luoyang 471023, China
[2] Luoyang Ship Material Research Institute, Luoyang 471023, China
[3] School of Materials Science and Chemical Engineering, Harbin University of Science and Technology, Harbin 150080, China
* Correspondence: jiangwei@hrbust.edu.cn (W.J.); cljie725@163.com (L.C.)

Abstract

$CoCrNiTiAl_x$ high-entropy alloy films with varied Al contents were fabricated on 42CrMo steel substrates via magnetron sputtering. By adjusting the sputtering power of the Al target, an investigation was systematically carried out to explore the effect of different Al contents on the microstructural evolution, mechanical properties, and corrosion resistance of the film, with the underlying synergistic mechanism governing these properties being elucidated. With increasing Al content, the film microstructure gradually transforms from an amorphous phase at low Al contents to a nanocrystalline–amorphous composite structure, until it is converted into the BCC phase, and the film's crystallinity exhibits a trend of first increasing and then decreasing. In terms of mechanical properties, the film hardness is significantly enhanced from 7.6 ± 1.3 GPa to 18.9 ± 1.1 GPa with increasing Al content, while the toughness gradually declines. Wear tests show that the film wear rate first decreases and then increases with rising Al content, reaching a minimum of 2.06×10^{-5} $mm^3/N{\cdot}m$. The superior protective state, characterized by a corrosion potential reaching −361.2 mV and corrosion current density dropping to 1.12 $\mu A/cm^2$, arises from the generation of an integrated, consistently structured composite passivation barrier in 3.5 wt.% solution. This study confirms that appropriate Al doping can synergistically optimize the microstructure, mechanical properties, and corrosion resistance of $CoCrNiTiAl_x$ films, providing experimental and theoretical support for the compositional design and engineering applications of high-performance high-entropy alloy protective films.

Keywords: high-entropy alloy film; phase transformation; mechanical properties; corrosion resistance

Check for updates

Academic Editors: Menachem Bamberger and Jiro Kitagawa

Received: 18 May 2026
Revised: 23 June 2026
Accepted: 1 July 2026
Published: 4 July 2026

Copyright: © 2026 by the authors. Licensee MDPI, Basel, Switzerland. This article is an open access article distributed under the terms and conditions of the Creative Commons Attribution (CC BY) license.

1. Introduction

In harsh industrial environments such as marine engineering and chemical processing, material surfaces often experience combined wear and corrosion. Traditional films, which excel in one aspect, typically fail to meet demanding service requirements. Therefore, the development of protective films that exhibit both outstanding wear resistance and superior corrosion resistance has become a critical need to address complex operational conditions [1]. A revolutionary multi-principal-element methodology serves as the basis for high-entropy alloys (HEAs), showing significant promise in surpassing the performance limitations of conventional alloys [2,3].

In engineering protection theory, films are commonly employed to enhance substrate performance and extend service life, owing to their high preparation efficiency and low cost [4,5]. For example, CoCrNi films exhibit corrosion resistance several times greater than that of traditional stainless steel. However, their relatively low hardness and wear resistance limit their application in wear-dominated environments [6,7]. Several strategies have been proposed to enhance the tribological properties of films, with alloy design-through the regulation of constituent element content being recognized as a direct approach to improve film performance. Magnetron sputtering is one of the leading methods for preparing alloy films, offering excellent process controllability, high adhesion between the film and substrate, and low defect density. Previous studies on CoNiVAl, CoCrNiAl, CoCrFeNiAl, and CoCrFeAl films have shown that Al can promote the formation of a body-centered cubic (BCC) phase, refine the grain structure to enhance film hardness, strengthen interfacial bonding, and impart high hardness, as well as superior strength, toughness, wear resistance, and thermal stability [8–11].

On this basis, extensive research has been conducted on the synergistic optimization of Ti and Al. Giljean et al. fabricated a series of TiAl/TiAlN-composite-structured films and found that Ti provides stiffness and chemical stability, while Al enables solid solution strengthening. This allows TiAl/TiAlN films to form alternating nano-scale stacks with continuous transition layers, achieving synchronous optimization of hardness, toughness, and modulus. Zheng et al. reported that Ti and Al, with significant atomic radius differences and characteristics as strong passivating elements, drive VAlTiCrSi films into an amorphous state and markedly enhance corrosion resistance [12]. In studies on FeCrNiTiAl and NbMoCrTiAl films, Ti and Al synergistically stabilize the films in a BCC phase, refine grains, homogenize dislocations, and generate dense composite passivation films [13,14].

In CoCrNi alloy film systems, the research on doping Ti has confirmed that varying the Ti content can significantly improve film hardness and promote the formation of a compact and stable oxide film under corrosive conditions, which can effectively inhibit performance deterioration [15,16]. In further studies involving Al doping, Sha et al. reported the production of dual-phase CoCrNiTiAl coatings with nanotwinned structures via magnetron sputtering, achieving 9.5 GPa hardness and appreciable damage tolerance [17]. Jiang et al. prepared CoCrNiTiAl films by co-sputtering with controlled bias voltage and achieved optimized comprehensive properties at −80 V bias, including 12.5 GPa hardness and 1.32 $\mu A/cm^2$ corrosion current density, through the formation of nanocrystalline–amorphous composite structures [18]. The above studies collectively indicate that adding Al to a CoCrNiTi base can significantly affect the mechanical properties and corrosion resistance of the film; however, several limitations remain in research, requiring in-depth and systematic investigation. No study has yet systematically elucidated how varying the Al content quantitatively controls the microstructural evolution and synergistic optimization of the mechanical properties and corrosion resistance within CoCrNiTiAl film systems. In this study, $CoCrNiTiAl_x$ films with varying Al contents were prepared using multi-target magnetron sputtering. The aim of this work is to elucidate the relationship between the microstructure and properties of the films as influenced by Al content, uncover the underlying mechanisms of synergistic enhancement, and provide both theoretical and experimental support for the design of high-performance functional films suitable for harsh wear–corrosion environments.

2. Method

Using magnetron sputtering, $CoCrNiTiAl_x$ films were deposited on 42CrMo steel substrates and (100) single-crystal Si wafer (42CrMo steel substrate was used for property testing, while the Si wafer was used for crystal structure characterization). Surface prepa-

ration involved progressive grinding and polishing using abrasive papers, followed by ultrasonic degreasing in anhydrous ethanol and petroleum ether (15 min per solvent) to eliminate all surface impurities and oxide films. CoCrNi alloy target (purity $\geq$ 99.9 at.%), Ti target (purity $\geq$ 99.995 at.%), and Al target (purity $\geq$ 99.995 at.%) were used as sputtering materials. The system was evacuated to 5×10^{-3} Pa, then backfilled with Ar (45 sccm) to 1.0 Pa. A Ti transition layer was pre-deposited, followed by the main film at fixed parameters (CoCrNi: 120 W, Ti: 100 W, bias: −80 V, 2.5 h). Al content was controlled by varying Al target power (60, 90, 120, 150 W); each set of processes prepared 15 samples. Field-emission scanning electron microscopy (SEM, Thermo Fisher Scientific, APREO, Hillsboro, OR, USA) equipped with an energy-dispersive spectrometer (EDS) was used to analyze surface/cross-sectional morphologies, elemental distribution, and wear tracks. X-ray diffraction (XRD, X'Pert PRO, Panalytical, Almelo, The Netherlands) was employed to identify phase compositions with a scanning range of 20–65° and a scanning speed of 5°/min. A white light interferometer (ATOMETRICS, NA500, Shenzhen, China) and an ultra-depth field microscope (OLYMPUS, DSX1000, Tokyo, Japan) were utilized to quantify surface roughness and 3D wear track profile, respectively. A nanoindenter (KLA Tencor, G200, Milpitas, CA, USA) was applied to obtain hardness and modulus via the continuous stiffness method, with 5 valid points per film, averaged after excluding extreme values. A Vickers hardness tester (SHANGHAI, ML204T, Shanghai, China) was used to evaluate fracture toughness by indentation crack propagation under a 500 g load; all were tested 3 times to ensure repeatability. Tribological properties were assessed with a ball-on-disk tribometer (Hengxv, MPT-3G, Jinan, China), with a GCr15 steel ball as the counterpart, a normal load of 1 N, a rotating speed of 100 rpm, and a testing duration of 10 min in air; each sample of each component was tested 3 times to ensure repeatability.

Electrochemical behavior was analyzed using an electrochemical workstation (Bio-Logic, VMP3, Seyssinet-Pariset, France) in 3.5 wt.% NaCl solution. The 42CrMo steel substrate coated with $CoCrNiTiAl_x$ film was used as the working electrode, with an exposed area of 1.0 cm^2. Ag/AgCl and Pt foil served as the reference and counter electrodes, respectively. EIS was measured at 10 mHz–100 kHz (10 mV amplitude), followed by potentiodynamic polarization. Corrosion current density (i_{corr}) and corrosion potential (E_{corr})were obtained by Tafel extrapolation. All electrochemical tests were repeated three times to ensure data reliability.

3. Results and Discussion

3.1. Microstructure

Figure 1 shows the elemental composition of the films. The relative atomic proportions of the five constituent elements in the deposited films were all in line with the composition design criteria for HEAs. With an increase in aluminum target power, the atomic percentage of Al increases gradually from 6 at.% to 26 at.%, whereas the contents of the remaining elements show a declining trend. Based on the Al content, the four groups of films in this experiment were designated as TA6, TA11, TA20, and TA26, corresponding to Al contents of 6.48 at.%, 11.37 at.%, 20.04 at.%, and 26.03 at.%, respectively.

Figure 2a displays the surface morphologies of the films. The surface of the TA6 film shows spherical protrusions. These spherical protrusions are essentially uncoalesced structures composed of low-mobility atoms, and they assume a spherical shape due to surface tension [19]. The remaining films all exhibited uniform and dense surfaces, without any cracks or large protrusions, conforming to the characteristics of the magnetron sputtering process and exhibiting excellent surface quality. Figure 2b shows the surface elemental mapping of the TA26 film, revealing uniform elemental distribution without segregation [19]. Cross-sectional images of the films are shown in Figure 2c, where the film

thickness gradually increases with rising Al content. Figure 2d shows the deposition rate of the films. The deposition rate rises from 10.13 ± 0.18 nm/min to 12.26 ± 0.24 nm/min with increasing Al target power. With fixed powers of the CoCrNi and Ti targets, higher-power Al target raises the incident ion energy and the quantity of sputtered target atoms per unit time, which further improves the deposition rate and results in a thicker film [20].

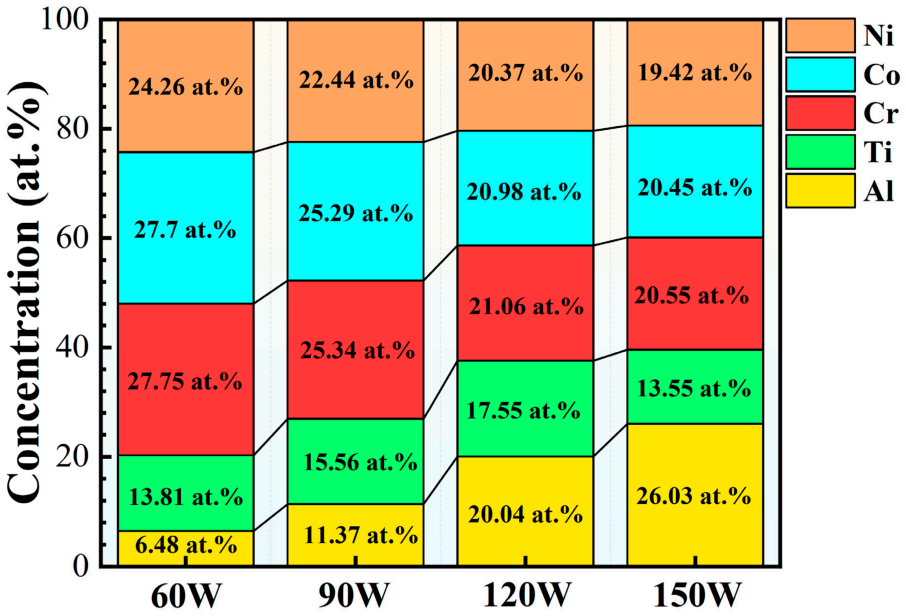


Figure 1. Chemical composition of $CoCrNiTiAl_x$ films under different Al target sputtering powers.

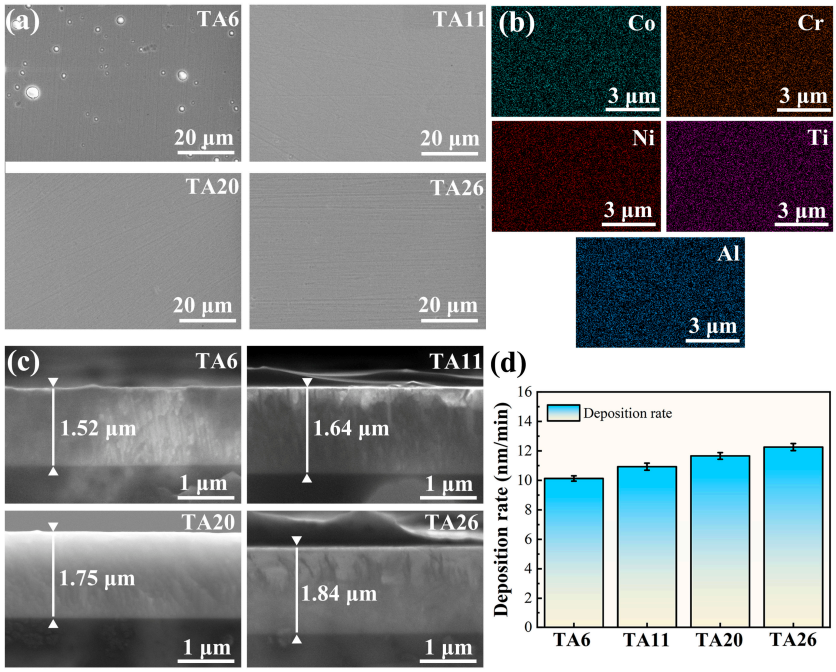


Figure 2. (**a**) Surface morphology, (**b**) surface element composition of TA26 film, (**c**) cross-sectional morphology, (**d**) deposition rates of $CoCrNiTiAl_x$ films.

Figure 3 shows the XRD patterns of $CoCrNiTiAl_x$ films at different Al target powers. The TA6 and TA11 films exhibit broad peaks representing an amorphous phase, indicating a dominant amorphous structure [16]. Figure 3 shows the XRD patterns of $CoCrNiTiAl_x$ films at different Al target powers. The TA6 and TA11 films exhibit broad humps representing an amorphous phase, indicating a dominant amorphous structure [20,21]. The large atomic

radius of Al increases the lattice distortion in the face-centered cubic (FCC) lattice. In contrast, the BCC lattice has a lower packing fraction and a looser structure, which can better accommodate large Al atoms. Therefore, increasing the Al content induces the phase transition of films from the FCC to BCC phase. The FCC peak of the TA26 film is relatively small, indicating that the crystal phase within the film is mainly composed of the BCC phase at this stage.

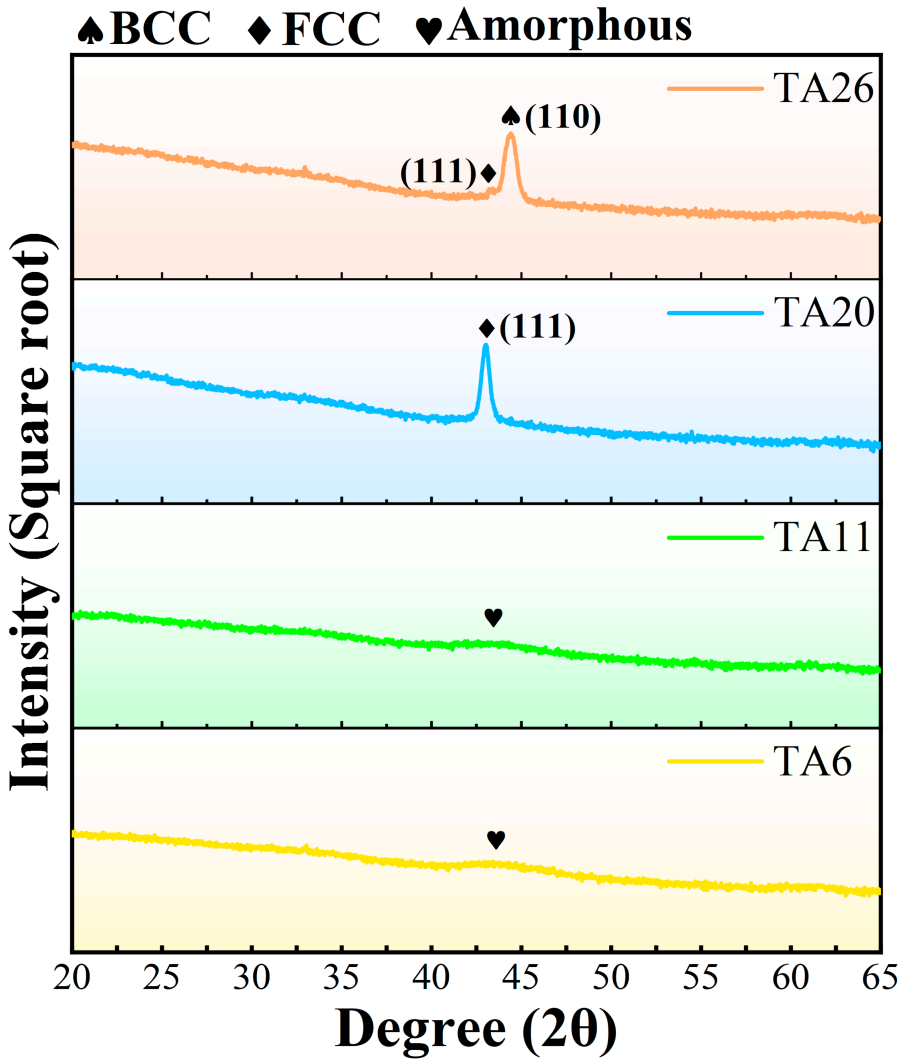


Figure 3. XRD patterns of $CoCrNiTiAl_x$ films.

The incident energy of particles during deposition can be described by the following equation:

$$U_k \propto D_w V_s / P_{0.5} \quad (1)$$

P is the gas pressure, V_s is the substrate bias, and D_w is the target power density. Under constant gas pressure (P) and substrate bias (V_s), the incident energy of the particles is positively correlated with the target power density (D_w). Table 1 lists lattice parameters, full width at half maximum (FWHM), grain size, and crystallinity of the films with different Al contents. These parameters could not be calculated for TA6 and TA11 films due to their amorphous structure. The film crystallinity first increases and then decreases with increasing Al content. When the Al target power increases from 60 W to 120 W, the elevated particle energy facilitates the migration of the adsorbed atoms toward stable lattice positions. This improvement enhances the crystallinity of the films and converts

the amorphous structure of TA6 and TA11 into a nanocrystalline–amorphous composite structure for TA20 film. Nevertheless, when the Al target power is further increased to 150 W, the excessive incident energy restricts the migration distance of the adsorbed atoms on the film surface, consequently reducing the crystallinity of the TA26 film. Meanwhile, the incorporation of large-radius Al atoms intensifies internal lattice distortion and increases defects, further lowering crystallinity. With increasing Al doping, the FWHM of the films increases, while the grain size and lattice constant decrease. Higher incident energy also promotes grain refinement. The lattice constants of TA20 and TA26 are 0.342 nm and 0.271 nm, corresponding to FCC and BCC solid solution structures, respectively.

Table 1. Lattice parameters, FWHM, grain size and crystallinity of $CoCrNiTiAl_x$ films.

Samples	Lattice Parameter (nm)	FWHM	Grain Size (nm)	Crystallinity (%)
TA6	-	-	-	-
TA11	-	-	-	-
TA20	0.342	0.429	20.5	88.12
TA26	0.271	0.626	13.9	75.36

The solid solution formation was evaluated via the thermodynamic parameter (Ω) and average atomic size difference (δ); valence electron concentration (VEC) predicts phase type and transitions. The Ω, δ, and VEC of the films were calculated using the following equations [3,13,22]:

$$\Delta H_{mix} = 4\sum_{i=0}^{n} \Delta H_{ij}^{mix} c_i c_j \quad (2)$$

$$\Delta S_{mix} = -R\sum_{i=1}^{N} c_i ln c_i \quad (3)$$

$$T_m = \sum_{i=1}^{n} c_i (T_m)_i \quad (4)$$

$$\delta = 100\sqrt{\sum_{i=1}^{n} c_i \left(1 - \frac{r_i}{\bar{r}}\right)^2}, \ \bar{r} = \sum_{i=1}^{n} c_i r_i \quad (5)$$

$$VEC = \sum_{i=1}^{n} c_i (VEC)_i \quad (6)$$

$$\Omega = \frac{T_m \Delta S_{mix}}{|\Delta H_{mix}|} \quad (7)$$

ΔH_{mix} is the mixing enthalpy, ΔH_{ij}^{mix} is the binary mixing enthalpy, c_i and c_j are the atomic fractions of elements i and j, ΔS_{mix} is the mixing entropy, T_m is the average melting point, R is the gas constant, n is the number of elements, $\bar{r}$ is the average atomic radius, r_i is the atomic radius of element i, and $(VEC)_i$ is the valence electron concentration of element i.

The calculated results are list in Table 2. HEAs form solid solutions when $\Omega > 1.1$ and $\delta < 6.6\%$. TA6 and TA11 have $\Omega < 1.1$ and $\delta > 6.6\%$, so they do not form solid solutions. More negative ΔH_{mix}, larger δ, and smaller ΔS_{mix} favor amorphous structures. TA20 and TA26 have $\Omega > 1.1$ and $\delta < 6.6\%$, favoring solid solutions, with $VEC \geq 8$ yielding FCC, and $6.9 \leq$ VEC < 8 yielding mixed FCC + BCC. TA20 ($VEC > 8$) tends to form FCC, while TA26 ($6.9 < VEC < 8$) may form mixed BCC + FCC.

Table 2. ΔS_{mix}, ΔH_{mix}, Ω, δ and *VEC* of $CoCrNiTiAl_x$ films.

Samples	ΔS_{mix} (J/K·mol)	ΔH_{mix} (KJ/mol)	Ω	δ (%)	*VEC*
TA6	12.52	−24.70	0.96	6.71	9.54
TA11	13.03	−23.73	0.92	6.77	9.03
TA20	13.36	−24.74	1.23	6.17	8.78
TA26	13.21	−24.22	1.28	5.99	7.37

3.2. Mechanical Properties

Figure 4a presents the nanoindentation load–displacement curves of the $CoCrNiTiAl_x$ films, which can be divided into regions of plastic deformation and elastic recovery [23]. The TA6 film exhibits the widest plastic deformation region and the narrowest elastic recovery region. As the Al content increases, the plastic deformation region narrows, while the elastic recovery region widens, indicating that the BCC structure formed by Al doping enhances the plastic deformation resistance of the prepared films. Figure 4b presents the hardness and elastic modulus of the samples, as well as the changing trends of the H/E and H^3/E^2 ratios. With the rise in Al content, the film hardness increases from 7.6 ± 1.3 GPa to 18.9 ± 1.1 GPa, and the elastic modulus grows from 147.1 ± 1.0 GPa to 227.0 ± 5.4 GPa. This phenomenon corresponds to a reduced plastic deformation region and an expanded elastic recovery region of the films. The TA26 film possesses the highest hardness and elastic modulus. According to the XRD results, the TA6 and TA11 films are primarily amorphous with numerous internal defects, resulting in typically low hardness. With the increase in Al content, the film undergoes a structural transition from a purely amorphous state to a nanocrystalline–amorphous composite structure, and the generation of nanocrystals contributes to the enhancement in film hardness. Furthermore, increasing Al content enhances internal lattice distortion, which raises the internal energy and stress within the films, further boosting the hardness. Finally, the TA26 film retains a nanocrystalline–amorphous composite structure, but the FCC solid-solution phase transforms into a BCC solid-solution structure due to the substantial influence of Al atoms. The BCC structure is characterized by strong interatomic bonding and complex slip behavior, which impedes dislocation motion and leads to a further increase in hardness.

To intuitively demonstrate the variation in film toughness with different Al contents, the energy toughness density (Γ_{ind}) and residual depth ratio (η) of the films with different compositions were calculated using the following equations [23]:

$$W_{tot} = \int_0^{h_{max}} P(h)dh \tag{8}$$

$$W_{el} = \int_{upload} P(h)dh \tag{9}$$

$$W_{pl} = W_{tot} - W_{el} \tag{10}$$

$$h_c = h_{max} - \varepsilon\frac{P_{max}}{S}, A_c = 24.5{h_c}^2 \tag{11}$$

$$\Gamma_{ind} = \frac{W_{pl}}{A_c} \tag{12}$$

$$\eta = \frac{h_{res}}{h_{max}} \tag{13}$$

W_{tot} is the total work, W_{el} is the elastic recovery work, W_{pl} is the plastic work, S is the contact stiffness (initial slope of the unloading curve), h_c is the contact depth, h_{max} is the maximum indentation depth, P_{max} is the maximum load, ε is the geometric correction

factor (0.75 for Berkovich indenter, A_c is the contact area, and h_{res} is the residual depth after complete unloading. The calculated results are shown in Figure 4c. Γ_{ind} reflects the ability of materials to resist crack initiation and propagation under local loading; a higher value indicates stronger crack resistance and toughness. η describes the elastic recovery ability of materials during unloading: a value close to one indicates dominant plastic deformation, while a smaller value represents a higher proportion of elastic recovery [24]. TA20 exhibits the highest Γ_{ind} and lowest η, demonstrating outstanding comprehensive mechanical properties. This indicates that the film can absorb more deformation energy under external loads while maintaining excellent elastic recovery, effectively suppressing crack initiation and propagation with high hardness [25].

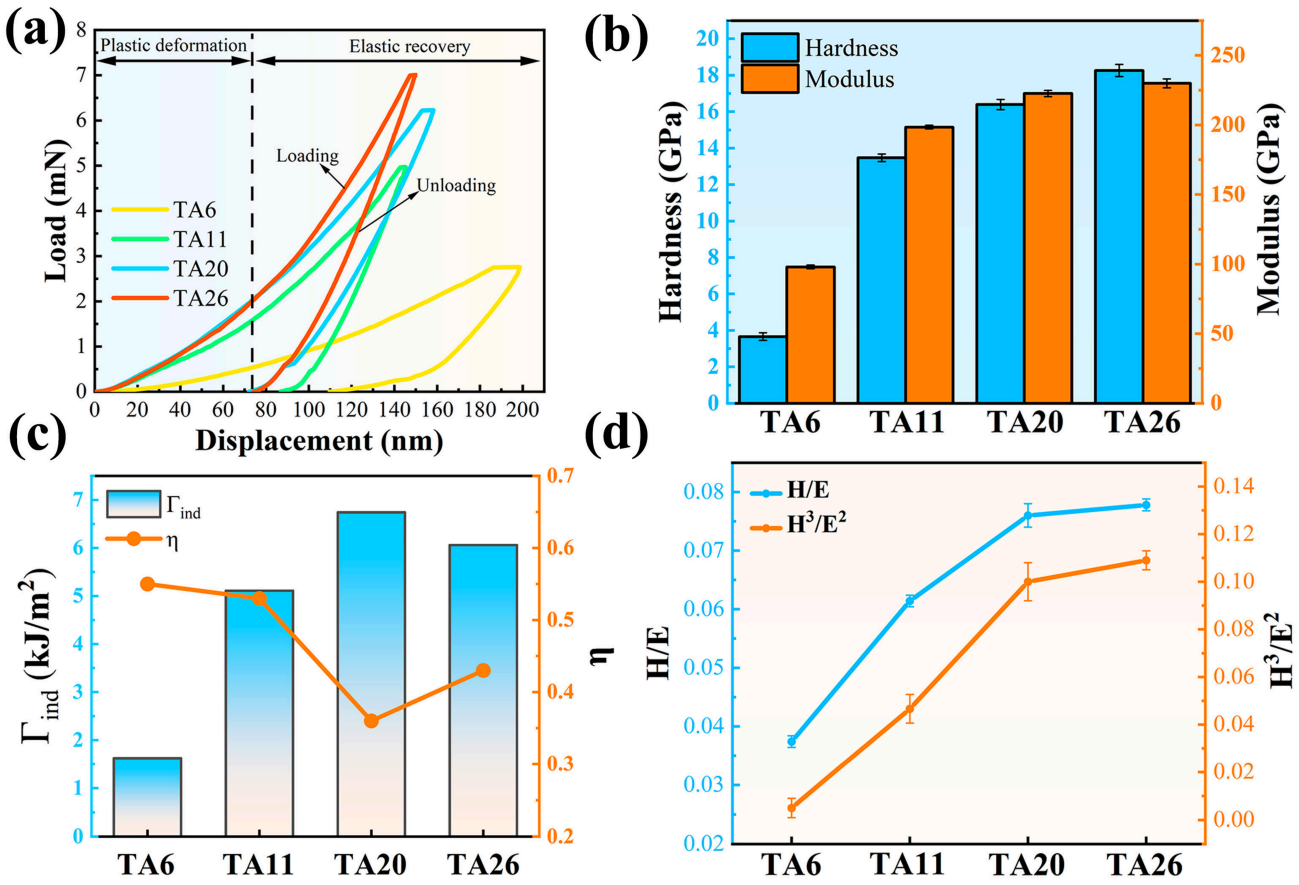


Figure 4. (**a**) Load–depth curves, (**b**) hardness and modulus, (**c**) energy toughness density and residual depth ratio, (**d**) H/E and H^3/E^2 of $CoCrNiTiAl_x$ films.

Figure 4d demonstrates the changes in the H/E and H^3/E^2 ratios of the films with increasing Al contents, both of which exhibit a gradual upward tendency. The H/E ratio is indicative of the film's elastic deformation recovery capacity, while the H^3/E^2 ratio is employed to assess its resistance to plastic deformation. Prior research has verified that higher H/E and H^3/E^2 values are associated with superior wear resistance of films. However, the wear resistance of films is not only determined by hardness and modulus; film toughness and film–substrate adhesion are also critical influencing factors [26].

The toughness of the films was evaluated by observing the length and distribution of the cracks around and inside the Vickers indentations, as illustrated in Figure 5. No visible cracks were observed around or within the indents of the TA6 and TA11 films, which correlates strongly with their low hardness and amorphous structure, indicating high crack propagation resistance [1,27]. The TA20 film displays a number of edge cracks near and around the indent, suggesting a transition from plastic to elastic deformation under loading.

The TA26 film exhibits a greater number of edge cracks both around and inside the indent, indicating a reduction in toughness. Overall, the toughness of the films gradually decreases with increasing Al content. The formation of a BCC structure in the TA26 film leads to a more brittle tendency and an increase in η, further deteriorating toughness.

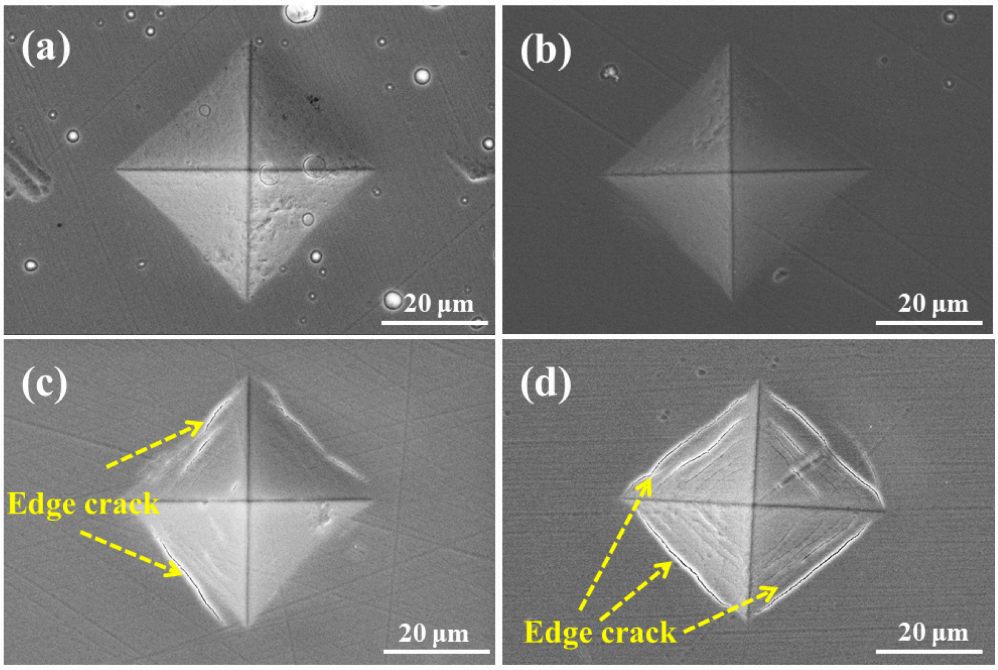


Figure 5. Vickers indentation morphology of $CoCrNiTiAl_x$ films: (**a**) TA6, (**b**) TA11, (**c**) TA20, (**d**) TA26.

The wear track morphologies after the friction and wear tests are shown in Figure 6. Figure 6a illustrates the significant fragmentation of the TA6 film. As seen in Figure 6(a1), the marked enrichment in Fe in the wear track indicates complete film failure and the loss of substrate protection. Figure 6b shows the partial peeling of the TA11 film, although most areas remain intact, as confirmed by the Fe distribution in Figure 6(b1). Figure 6c,d present the wear tracks of the TA20 and TA26 films, respectively, which exhibit no peeling and some protrusions. EDS analysis reveals no Fe enrichment, confirming that the films are not worn through.

The 3D and cross-sectional morphology of the wear track are shown in Figure 7a. For the TA6 film, the cross-sectional curve shows a pronounced deep groove with a maximum depth of approximately −2 μm centered, and the 3D view reveals a distinct wear track with significant material removal and scattered debris along the sliding direction. The TA11 film exhibits multiple peaks and valleys, including a sharp peak near 1 μm and deep troughs reaching −2 μm, while its 3D morphology displays a prominent ridge. In contrast, the TA20 film shows the shallowest and narrowest wear mark with minimal depth variation, and its 3D surface appears relatively smooth, with only fine scratches. The TA26 film demonstrates moderate wear behavior with a broad groove depth of about −1 μm and a 3D morphology characterized by a visible wear track with moderate surface roughening and some pile-up along the edges. As shown in Figure 7b, the wear track widths are 252.5 ± 9.48 μm for TA6, 213.0 ± 7.04 μm for TA11, 193.4 ± 9.69 μm for TA20 (the narrowest), and 324.6 ± 9.54 μm for TA26. The wear track width first decreases and then increases with rising Al content. The wear rate was calculated using the cross-sectional profile according to the following equation [28]:

$$K = V/(FD) \quad (14)$$

where V is the wear volume, F is the applied load, and D is the total sliding distance. The calculated results are plotted in Figure 7c. The wear rates of TA6, TA11, TA20, and TA26 are 16.61 × 10^{-5} mm^3/N·m, 10.81 × 10^{-5} mm^3/N·m, 2.06 × 10^{-5} mm^3/N·m, and 6.13 × 10^{-5} mm^3/N·m, respectively. The wear rate shows a trend of first decreasing and then increasing with rising Al content, and the TA20 film has the lowest wear rate, indicating the best tribological behavior.

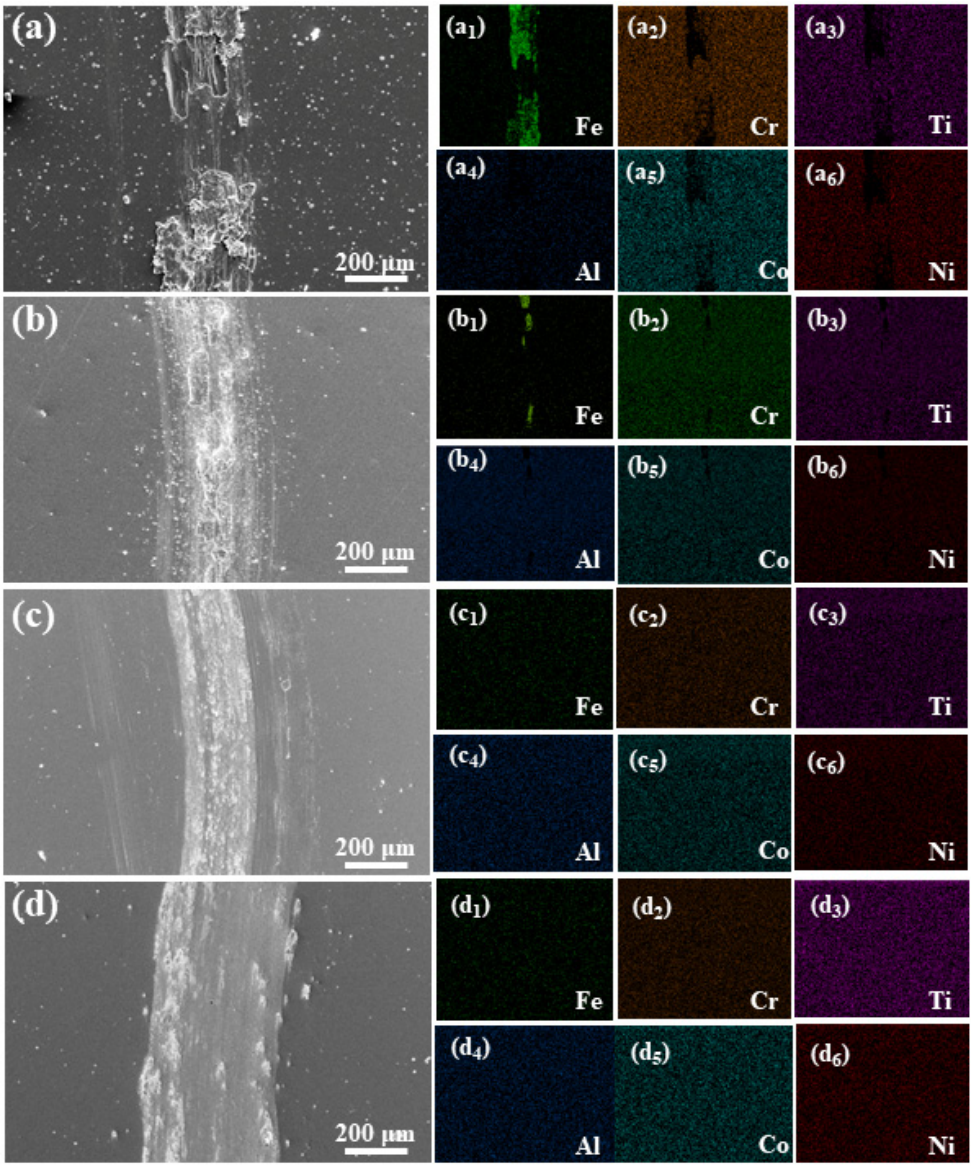


Figure 6. Morphology and elemental distribution of wear marks of $CoCrNiTiAl_x$ films: (**a**) TA6, (**b**) TA11, (**c**) TA20, (**d**) TA26; (**a_1–a_6**, **b_1–b_6**, **c_1–c_6**, **d_1–d_6**) corresponding EDS elemental mappings of Fe, Cr, Ti, Al, Co, and Ni.

To further investigate the wear characteristics of $CoCrNiTiAl_x$ films with different Al contents, micro-area wear track analysis was performed. The wear tracks with varying Al contents and the EDS spectrum s for selected regions are shown in Figure 8 and Table 3 respectively. In Figure 8a, obvious peeling is observed on the wear track surface of the TA6 film. Owing to its low hardness, the TA6 film struggles to resist the relative sliding of the counterpart, leading to surface accumulation, large-area peeling, and exposure of the underlying Fe substrate [29,30]. EDS detection performed on the peeled region (Region A) also reveals O enrichment, which suggests that the film undergoes oxidation during the

friction process. The wear characteristics further confirm that the wear mechanisms of the TA6 film consist of adhesive wear and oxidative wear. Figure 8b shows a large adhesive layer and abrasive agglomerates on the wear track surface of TA11 without large-area peeling, improving tribological performance. EDS analysis of the adhesive area (Region B) reveals O enrichment, indicating that the wear mechanisms of TA11 are abrasive wear, adhesive wear, and oxidative wear. Figure 8c displays the micro-area wear morphology of TA20, with small adhesive areas and few abrasives, indicating further improvements in tribological performance. The EDS analysis of Region C revealed O content in the adhesive area is low, and the main wear mechanism of TA20 is abrasive wear [15,31]. Figure 8d shows the micro-area wear morphology of TA26, with a large adhesive layer but no obvious abrasives, indicating adhesive wear is dominant. EDS analysis of Region D shows high O content in the adhesive area, suggesting the occurrence of oxidative wear.

In summary, increasing the Al content significantly affects the mechanical properties of the films by altering the microstructure, which further influences tribological performance. The tribological properties are jointly determined by film hardness, toughness, and substrate adhesion. The TA6 and TA11 films are fully amorphous, with strong crack propagation resistance but low hardness, resulting in poor wear resistance. With increasing Al content, the TA20 and TA26 films transform into an nanocrystalline–amorphous composite structure, where embedded nanocrystals enhance hardness and adhesion, thereby improving wear resistance. However, excessive Al content induces high residual stress, increases η, triggers the phase transition from FCC to BCC. Although this enhances hardness, BCC lattice features are lower than those of FCC, operating with limited slip systems. The research by Sun et al. indicates that under wear sliding contact, the restricted plastic deformation capacity of the BCC phase cannot accommodate the shear stress generated at the asperity level, leading to stress accumulation and subsequent brittle fracture [32].

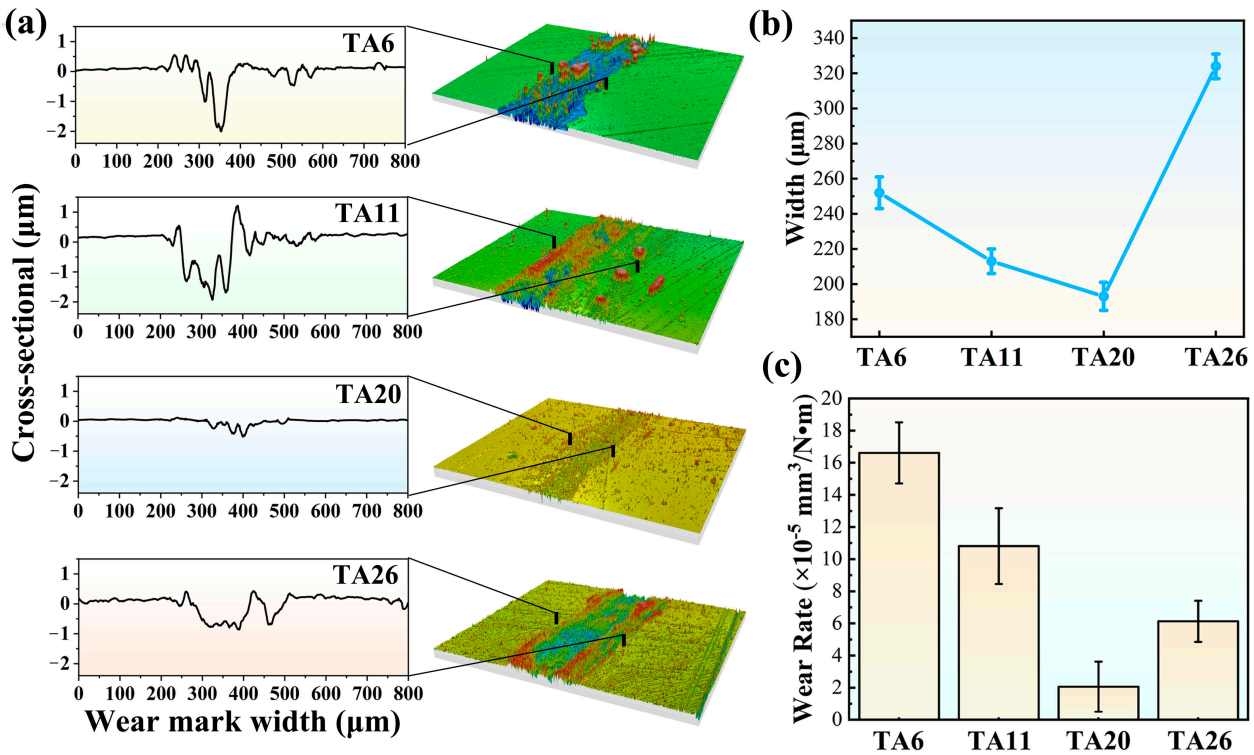


Figure 7. Morphology, wear width, and wear rate of $CoCrNiTiAl_x$ films: (**a**) cross-sectional curves and corresponding 3D surface morphologies of wear marks for TA6, TA11, TA20, and TA26; (**b**) wear mark width; (**c**) wear rate.

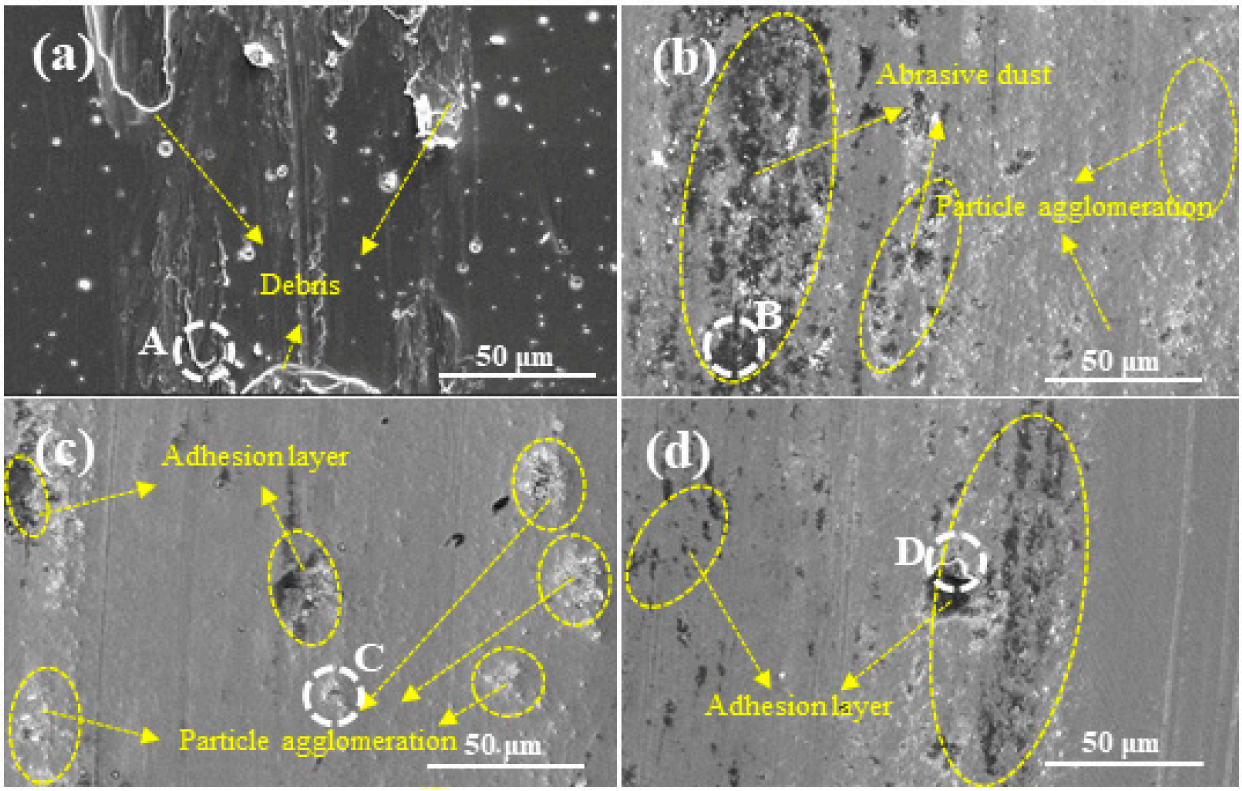


Figure 8. Wear surface morphology of $CoCrNiTiAl_x$ films deposited with different Al contents: (**a**) TA6, (**b**) TA11, (**c**) TA20, (**d**) TA26.

Table 3. Elemental composition of micro-region.

	Co	Cr	Ni	Ti	Al	O
TA6	0.53	5.2	4.5	3.74	4.19	81.85
TA11	12.61	11.86	12.15	11.64	8.49	43.25
TA20	17.56	16.87	17.12	13.86	15.77	18.81
TA26	13.67	13.72	12.89	11.46	11.57	34.48

3.3. Corrosion Resistance

Figure 9 presents the potentiodynamic polarization curves of the $CoCrNiTiAl_x$ films with different Al contents, which were deposited in a 3.5 wt.% NaCl solution. The polarization resistance (R_p) was calculated using the Stern–Geary equation [33]:

$$i_{corr} = \frac{\beta_a \beta_c}{2.303 \times R_p(\beta_a + \beta_c)} \quad (15)$$

where β_a and β_c are the slopes of the anodic and cathodic curves, respectively, and R_p is the polarization resistance. Table 4 lists the calculated E_{corr}, i_{corr}, and R_p. The potentiodynamic polarization curves reveal distinct electrochemical behaviors for each composition. For the TA6 film, the curve exhibits the most negative corrosion potential (E_{corr}) is −817.3 mV, and the highest corrosion current density (i_{corr}) is 8.22 μA/cm^2, which is close to that of the substrate, which has an E_{corr} reach −849.4 mV, indicating the continuous active dissolution of the surface. The TA11 film shows improvement, with its E_{corr} shifting positively to −741.5 mV and i_{corr} decreasing to 5.97 μA/cm^2; high corrosion current density indicates limited film stability. The TA20 film demonstrates the optimal corrosion performance, featuring the most positive E_{corr} of −361.2 mV and the lowest i_{corr} of 1.12 μA/cm^2; the i_{corr} gradually increases with the increase in the potential of the passive region. The current

fluctuations in this region arise from the competition between passive film formation and dissolution [34]. The highest polarization resistance is 8.64 × 10^5 Ω·cm^2. In contrast, TA26 exhibits a noticeably broad passive plateau spanning a wide potential range, yet has a higher corrosion current density of 1.96 μA/cm^2 and a lower polarization resistance of 5.76 × 10^3 Ω·cm^2 compared to TA20. This combination suggests that while a passive film does form, its elevated passive current indicates a more porous or less compact film structure with inferior protective efficiency despite its extended stability stage.

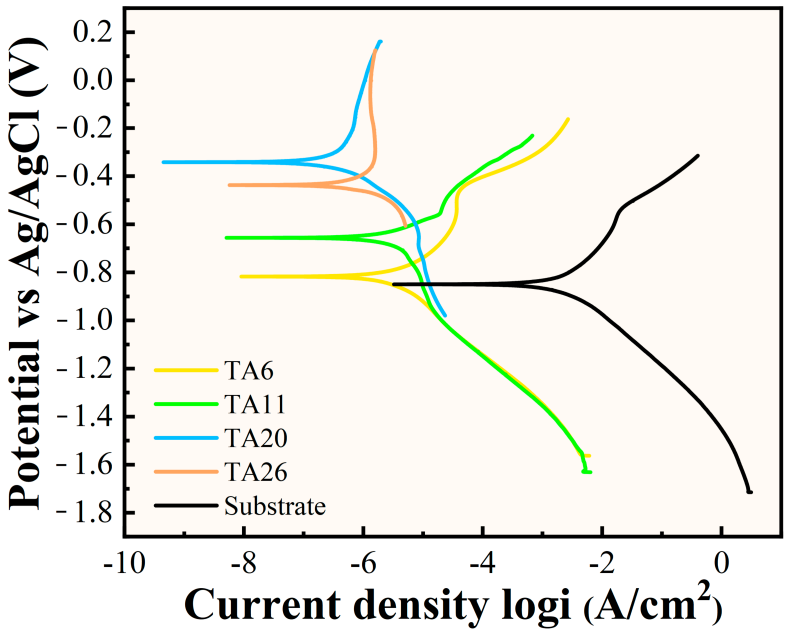


Figure 9. Potentiodynamic polarization curves of $CoCrNiTiAl_x$ films.

Table 4. Corrosion parameters of $CoCrNiTiAl_x$ films and substrate.

Negative Bias Voltage (V)	E_{corr} (mV)	βa (mV)	βc (mV)	i_{corr} (μA/cm^2)	R_p (Ω·cm^2)
TA6	−817.3	310.7	445.2	8.22	6.52 × 10^3
TA11	−741.5	396.7	465.8	5.97	8.35 × 10^3
TA20	−361.2	617.5	114.2	1.12	8.64 × 10^4
TA26	−437.1	512.3	110.5	1.96	5.76 × 10^4
Substrate	−849.4	388.8	257.8	12.47	5.39 × 10^3

EIS tests were conducted on $CoCrNiTiAl_x$ films with different Al contents, and the results are shown in Figure 10. In Figure 10a, the diameter of the arc in the Nyquist plot is indicative of the films' corrosion resistance [1,28,35]. As the Al content increases, the arc diameter first rises then falls, indicating corrosion resistance follows the same pattern. Figure 10b displays the Bode modulus diagrams, in which the low-frequency |Z| magnitude characterizes the corrosion resistance of the film samples [1]. Among all the film samples, TA20 demonstrates a favorable combination of corrosion resistance within the current composition window. Figure 10c presents a phase angle diagram, which reveals the presence of two time constants during the corrosion process; this phenomenon indicates that two interfacial reactions occur during corrosion. In general, the height of the capacitance peak is indicative of the corrosion resistance of the films, which is consistent with the variation trend observed in the Nyquist plots [36]. The equivalent circuit is shown in Figure 10d; considering the evolution of asymmetric Bode and phase angle plots, the $R_s(Q_p(R_f(Q_{dl}R_{ct}))$ is preferentially utilized to fit the EIS data for the double-layered structure

of passivated films on the sample surface. Consisting of solution resistance (R_s), passive film resistance (R_f), and charge transfer resistance (R_{ct}), Q_p represents film capacitance, and Q_{dl} represents double-layer capacitance [1]. The fitting results are listed in Table 5. The solution resistance R_s shows little variation, indicating the good stability of the testing system. The main parameters determining corrosion resistance are R_f and R_{ct}, and their sum represents the overall corrosion resistance of the sample. The $R_f + R_{ct}$ values of TA6, TA11, TA20, and TA26 are 4.88 × 10^3 Ω·cm^2, 5.97 × 10^3 Ω·cm^2, 4.95 × 10^4 Ω·cm^2, and 2.11 × 10^4 Ω·cm^2, respectively. The TA20 film has the largest $R_f + R_{ct}$ and the best corrosion resistance. These can be attributed to the enrichment in Al on the film surface, forming a passivation film mainly composed of Al oxides and hydroxides that provide corrosion protection. With increasing Al content, the passivation film becomes thicker and denser, offering better protection. However, the corrosion resistance of TA26 decreases, which may be due to the excessive Al content altering the internal grain boundary structure and the crystalline phase transforming the FCC phase of the TA20 film into the BCC phase of the TA26 film. Previous studies have confirmed that FCC-structured films feature high compactness, uniformity, and passivation film self-repair ability, exhibiting superior corrosion resistance, while BCC structures have loose atomic packing, low packing density, and high defect density, leading to poor corrosion resistance.

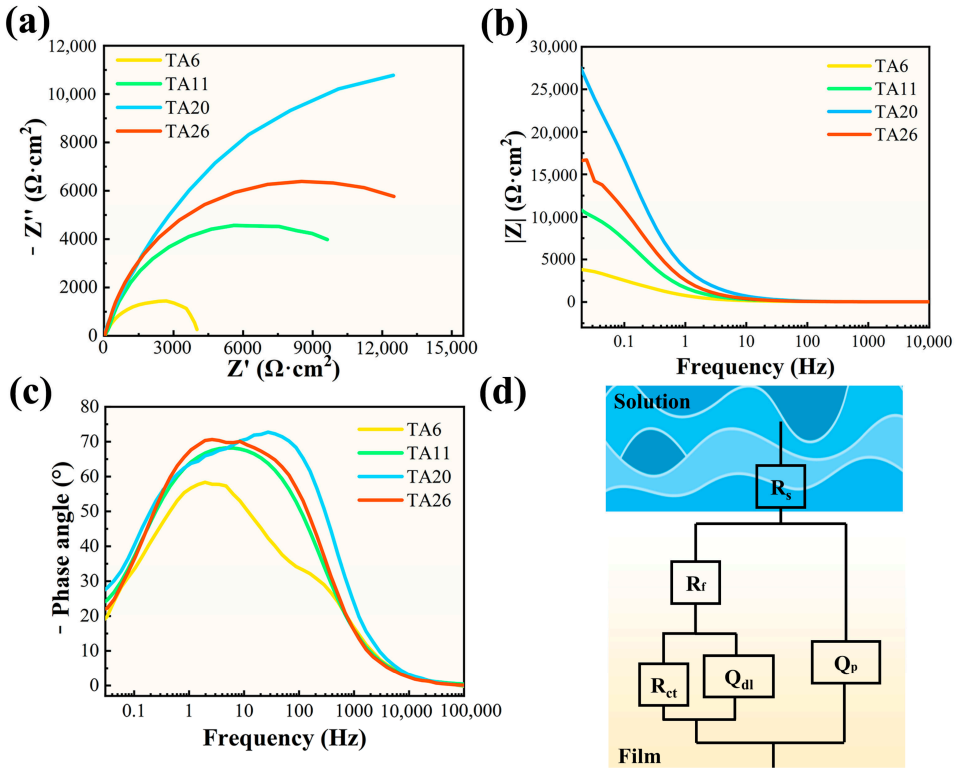


Figure 10. (**a**) Nyquist plots, (**b**) Bode diagram, (**c**) phase angle, (**d**) fitted circuit diagram of $CoCrNiTiAl_x$ films.

Table 5. Impedance fitting results of $CoCrNiTiAl_x$ films.

Negative Bias Voltage (V)	R_s (Ω·cm^2)	R_f (Ω·cm^2)	Q_P (F·s^n·cm^{-2})	n_c	R_{ct} (Ω·cm^2)	Q_{dl} (F·s^n·cm^{-2})	n_{dl}	χ^2
TA6	23.22	4.58 × 10^2	3.94 × 10^{-5}	0.91	4.30 × 10^3	2.93 × 10^{-4}	0.73	4.7 × 10^{-4}
TA11	26.19	6.23 × 10^2	4.60 × 10^{-5}	0.88	5.35 × 10^3	4.26 × 10^{-4}	0.77	1.9 × 10^{-3}
TA20	24.08	9.36 × 10^3	2.54 × 10^{-5}	0.86	4.02 × 10^4	4.34 × 10^{-5}	0.86	8.5 × 10^{-4}
TA26	24.89	1.65 × 10^3	7.89 × 10^{-5}	0.84	1.95 × 10^4	1.21 × 10^{-4}	0.99	7.9 × 10^{-4}

Increasing Al content induces phase transitions in films. TA6 and TA11 are amorphous, TA20 has a nanocrystalline–amorphous composite structure with FCC crystalline phase, and TA26 features a nanocrystalline–amorphous composite structure with a BCC + FCC crystalline phase. The composite structure improves mechanical properties and plastic deformation resistance, further enhancing wear resistance. Meanwhile, rising the Al content promotes the formation of a dense oxide film on the film surface, improving corrosion resistance. Previous studies indicate that moderate Al addition enhances corrosion resistance by forming a dense, stable, Al_2O_3-rich passive film with reduced defect density [34]. However, excessive Al or multiphase microstructures can induce phase segregation and porosity, thereby compromising the film's protective capability [37].

4. Conclusions

$CoCrNiTiAl_x$ films were fabricated using multi-target magnetron sputtering with varying Al target powers. The influences of Al target sputtering power on the microstructures and properties of the deposited films were systematically studied. The key research findings are as follows:

1. The Al content plays a key role in controlling the film's microstructure. When the Al target power rises from 60 W to 150 W, the films gradually transition from an amorphous state to an amorphous–BCC + FCC composite structure, and their crystallinity first increases and then decreases.
2. The hardness of the films is significantly enhanced with increasing Al content, reaching 18.9 $\pm$ 1.1 GPa for the TA26 film with 26 at.% Al. Toughness gradually decreases with rising Al content, with the TA20 film (20 at.% Al) achieving the optimal balance between hardness and toughness.
3. The tribological performance of the $CoCrNiTiAl_x$ films is synergistically influenced by hardness and toughness. The TA20 film exhibits the lowest wear rate, with abrasive wear being the dominant mechanism. Excessive Al content in the TA26 film reduces its toughness and film–substrate adhesion, resulting in a slight decline in wear performance.
4. Corrosion resistance initially increases and then decreases with increasing Al content. The TA20 film demonstrates the best corrosion resistance due to the formation of a dense amorphous–FCC composite structure and a stable passivation film, exhibiting the highest polarization resistance and charge transfer resistance. Excessive Al content induces phase transition to an amorphous-BCC + FCC composite structure, reducing compactness and deteriorating corrosion resistance.

Author Contributions: Conceptualization, L.C.; data curation, L.H., Z.L. and X.S.; formal analysis, L.H., Z.L., X.S. and L.L.; funding acquisition, W.J.; methodology, W.J. and L.C.; supervision, L.C.; validation, X.S. and L.L.; visualization, L.H. and Z.L.; writing—original draft, L.H., Z.L. and W.J.; writing—review and editing, W.J. All authors have read and agreed to the published version of the manuscript.

Funding: This work was supported by Heilongjiang Provincial Natural Science Foundation of China (LH2020E084).

Data Availability Statement: The raw data supporting the conclusions of this article will be made available by the authors on request.

Conflicts of Interest: The authors declare no conflicts of interest.

References

1. Yang, W.; Shen, J.; Wang, Z.; Ma, G.; Ke, P.; Wang, A. Mechanical and Electrochemical Properties of (MoNbTaTiZr)1-N High-Entropy Nitride Coatings. *J. Mater. Sci. Technol.* **2025**, *208*, 78–91. [CrossRef]
2. Yan, X.; Liaw, P.K.; Zhang, Y. Order and Disorder in Amorphous and High-Entropy Materials. *Met. Mater. Trans. A* **2021**, *52*, 2111–2122. [CrossRef]
3. Yeh, J.-W. Alloy Design Strategies and Future Trends in High-Entropy Alloys. *JOM* **2013**, *65*, 1759–1771. [CrossRef]
4. Garg, R.; Gonuguntla, S.; Sk, S.; Iqbal, M.S.; Dada, A.O.; Pal, U.; Ahmadipour, M. Sputtering Thin Films: Materials, Applications, Challenges and Future Directions. *Adv. Colloid Interface Sci.* **2024**, *330*, 103203. [CrossRef] [PubMed]
5. Jiang, W.; Jiang, Y.; Li, Z.; Wang, Z.; Liu, Y.; Wang, E.; Zhao, F. Effect of Nitrogen Doping on Microstructure, Mechanical Properties and Corrosion Resistance of CoCrFeNiCuNx High-Entropy Alloy Thin Films. *J. Alloys Compd.* **2025**, *1039*, 183395. [CrossRef]
6. Mohamed, O.; Hassan, M.; Egilmez, M.; Abuzaid, W.; Ibrahim, T.; Khamis, M. Corrosion Behavior of CoCrNi/Mild Steel Medium Entropy Alloy Thin Films. *Mater. Today Commun.* **2022**, *30*, 103015. [CrossRef]
7. Bajpai, S.; MacDonald, B.E.; Rupert, T.J.; Hahn, H.; Lavernia, E.J.; Apelian, D. Recent Progress in the CoCrNi Alloy System. *Materialia* **2022**, *24*, 101476. [CrossRef]
8. Wang, N.; Cao, Q.; Wang, X.; Ding, S.; Zhang, D.; Jiang, J.-Z. Ultrahigh Specific Hardness of Co-Ni-V-Al Medium Entropy Alloy Thin Films. *Mater. Today Commun.* **2022**, *31*, 103447. [CrossRef]
9. Sun, S.; Zai, W.; Chen, Y.; Huang, L.; Sun, G.; Lian, J. Effect of Al Addition on the Microstructure and Mechanical Properties of Al_x CrCoNi Medium Entropy Alloys Prepared via the Magnetron Co-Sputtering. *Adv. Eng. Mater.* **2022**, *24*, 2101529. [CrossRef]
10. Guan, Z.; Nan, S.; Feng, C.; Xiao, M.; Song, H.; Qin, G.; Guo, H.; Wu, L.; Gou, H.; Ma, D.; et al. Multicomponent Intermetallic Compound CoCrFeNiSi: Crystal Structure and Magnetic Properties. *J. Magn. Magn. Mater.* **2024**, *606*, 172401. [CrossRef]
11. Han, X.T.; Ma, Y.J.; Ma, H.; Chen, J.H.; Li, P.Y.; Zhang, Z.Y.; Zhang, Y.W.; Li, G.J.; Hu, J.B.; Cao, Z.H. Phase Transformation and Strengthening Effect Induced by Al Doping and Annealing in Nanostructural Medium Entropy Alloy Films. *Vacuum* **2023**, *215*, 112306. [CrossRef]
12. Zheng, S.; Cai, Z.; Pu, J.; Zeng, C.; Chen, S.; Chen, R.; Wang, L. A Feasible Method for the Fabrication of VAlTiCrSi Amorphous High Entropy Alloy Film with Outstanding Anti-Corrosion Property. *Appl. Surf. Sci.* **2019**, *483*, 870–874. [CrossRef]
13. Yu, S.; Sun, Y.; Tong, B.; Wang, T.; Wang, C.; Zhang, G. Fretting Wear Behavior of NbMoCrTixAly High Entropy Alloy Films Prepared by Magnetron Sputtering on Ti6Al4V Titanium Alloy. *J. Alloys Compd.* **2025**, *1034*, 181367. [CrossRef]
14. Wang, K.; Liu, M.; Liu, C.; Li, X.; Shao, G. Microstructure Evolution Mechanism and Corrosion Resistance of FeCrNi(AlTi)x Medium Entropy Alloy Prepared by Laser Melting Deposition with Al and Ti Content Changes. *Coatings* **2025**, *15*, 851. [CrossRef]
15. Jiang, W.; Ju, J.; Li, Z.; Wang, Z.; Wang, E.; Zhao, F. Synergetic Effect of Bias Voltage on Tribological Properties and Corrosion Behavior of CoCrNiTi Medium Entropy Alloy Films Deposited by Magnetron Sputtering. *Surf. Coat. Technol.* **2025**, *512*, 132380. [CrossRef]
16. Li, Z.; Jiang, W.; Liu, Y.; Wang, E.; Wang, Z.; Zhao, F.; Dai, H. Wear and Corrosion Performance of CoCrNiTi Medium Entropy Alloy Films: A Magnetron Sputtered Architecture from Crystal to Amorphous. *Surf. Coat. Technol.* **2026**, *519*, 132931. [CrossRef]
17. Sha, C.; Zhou, Z.; Xie, Z.; Munroe, P. Enhancing the Hardness and Damage-Tolerance of CoCrNiAlTi Coatings through Dual-Phase and Nanotwinned Structures. *Surf. Coat. Technol.* **2022**, *440*, 128479. [CrossRef]
18. Jiang, W.; Shen, X.; Jiang, Y.; Li, Z.; Wang, Z.; Wang, E.; Zhao, F. Investigation of the Effect of Substrate Bias on the Microstructure and Properties of Magnetron Sputtered CoCrNiTiAl High-Entropy Alloy Films. *Mater. Today Commun.* **2025**, *46*, 112700. [CrossRef]
19. Anders, A. Equilibrium and Non-Equilibrium Heating in Plasma-Based Deposition of Thin Films and Coatings. *Surf. Coat. Technol.* **2026**, *520*, 132946. [CrossRef]
20. Agustianingrum, M.P.; Yoshida, S.; Tsuji, N.; Park, N. Effect of Aluminum Addition on Solid Solution Strengthening in CoCrNi Medium-Entropy Alloy. *J. Alloys Compd.* **2019**, *781*, 866–872. [CrossRef]
21. Lu, W.; Luo, X.; Yang, Y.; Zhang, J.; Huang, B. Effects of Al Addition on Structural Evolution and Mechanical Properties of the CrCoNi Medium-Entropy Alloy. *Mater. Chem. Phys.* **2019**, *238*, 121841. [CrossRef]
22. Takeuchi, A.; Inoue, A. Classification of Bulk Metallic Glasses by Atomic Size Difference, Heat of Mixing and Period of Constituent Elements and Its Application to Characterization of the Main Alloying Element. *Mater. Trans.* **2005**, *46*, 2817–2829. [CrossRef]
23. He, M.; Li, F.; Cai, J.; Chen, B. An Indentation Technique for Estimating the Energy Density as Fracture Toughness with Berkovich Indenter for Ductile Bulk Materials. *Theor. Appl. Fract. Mech.* **2011**, *56*, 104–111. [CrossRef]
24. Chen, J.; Bull, S.J. Assessment of the Toughness of Thin Coatings Using Nanoindentation under Displacement Control. *Thin Solid. Films* **2006**, *494*, 1–7. [CrossRef]
25. Wang, K.; Zou, X.; Huang, G.; Zhang, R.; Yuan, K.; Yao, X. Strain-Rate-Dependent Behaviors of CoCrNiSi02 Medium-Entropy Alloy: Deformation Mechanism and Microstructural-Based Constitutive Modeling. *J. Alloys Compd.* **2023**, *968*, 171907. [CrossRef]
26. Chen, X.; Du, Y.; Chung, Y.-W. Commentary on Using H/E and H/E as Proxies for Fracture Toughness of Hard Coatings. *Thin Solid Films* **2019**, *688*, 137265. [CrossRef]

27. Obeydavi, A.; Shafyei, A.; Lee, J.-W. Investigating of the Microstructure, Mechanical Properties and Corrosion Behavior of CoCrFeMnNiSix High Entropy Alloy Thin Films Deposited by Co-Sputtering Method. *J. Alloys Compd.* **2025**, *1017*, 178972. [CrossRef]
28. Jiang, X.; Liu, W.; Huang, J.; Leng, Y. Achieving Superior Wear and Corrosion Resistance in FeCoNiCrNC Films via Nitrogen and Carbon Dual Anions Incorporation. *Appl. Surf. Sci.* **2025**, *682*, 161722. [CrossRef]
29. Gloriant, T. Microhardness and Abrasive Wear Resistance of Metallic Glasses and Nanostructured Composite Materials. *J. Non-Cryst. Solids* **2003**, *316*, 96–103. [CrossRef]
30. Patil, S.P.; Heider, Y. A Review on Brittle Fracture Nanomechanics by All-Atom Simulations. *Nanomaterials* **2019**, *9*, 1050. [CrossRef] [PubMed]
31. Yan, L.; Mei, S.; Cai, Z.; Liu, Y.; Wang, B.; Gu, L. Microstructure and Tribological Properties of (AlCrTiV)Nx High-Entropy Alloy Films Prepared by Magnetron Sputtering. *Surf. Coat. Technol.* **2025**, *512*, 132406. [CrossRef]
32. Sun, H.; Xin, B.; Chen, J.; Shi, P.; Yi, G.; Wan, S.; Meng, J.; Wang, W.; Shan, Y. Effect of the High Temperature Phase Transition on the Tribological Behavior of Atmospheric Plasma Sprayed AlCoCrFeNi-Bi2O3 Coating. *Surf. Coat. Technol.* **2024**, *476*, 130286. [CrossRef]
33. Qian, J.; Gao, Q.; Chen, X.; Wang, Q.; Huang, W.; Zhao, G.; Shen, J.; Zhou, Z.; Zhou, F. Electrochemical and Tribological Properties of Different NbMoSiN Composite- and Gradient- Films in Simulated Body Fluids. *Tribol. Int.* **2025**, *204*, 110456. [CrossRef]
34. Pan, Z.; Luo, H.; Zhao, Q.; Cheng, H.; Wei, Y.; Wang, X.; Zhang, B.; Li, X. Tailoring Microstructure and Corrosion Behavior of CoNiVAlx Medium Entropy Alloys via Al Addition. *Corros. Sci.* **2022**, *207*, 110570. [CrossRef]
35. Abegunde, O.O.; Makha, M.; Machkih, K.; Larhlimi, H.; Ghailane, A.; Samih, Y.; Alami, J. Structural, Mechanical and Corrosion Resistance of Phosphorus-Doped TiAlN Thin Film. *J. Mater. Sci.* **2022**, *57*, 19107–19130. [CrossRef]
36. Huang, D.; Xu, Z.; He, Y.; Liu, M.; Jia, X.; Zhou, T. Corrosion and Wear Resistance of HVOF-Sprayed Ni-Cr-Co Multi-Principal Element Alloy Coating on Copper Plate. *J. Therm. Spray Tech.* **2024**, *33*, 1585–1600. [CrossRef]
37. Gu, X.-H.; Li, X.-R.; Zhang, Q.-H.; Wu, L.-K.; Cao, F.-H. Passive Film and Surface Characterization of Alx(CoCrFeNi)100-x (x = 0, 5, 10, 15, 20) High Entropy Alloys. *Intermetallics* **2023**, *162*, 107994. [CrossRef]

Disclaimer/Publisher's Note: The statements, opinions and data contained in all publications are solely those of the individual author(s) and contributor(s) and not of MDPI and/or the editor(s). MDPI and/or the editor(s) disclaim responsibility for any injury to people or property resulting from any ideas, methods, instructions or products referred to in the content.